Journal of MATERIALS RESEARCH

Invited Feature Paper
DOI:10.1557/s43578-022-00838-1

Microstructural and mechanical properties of AlSi10Mg: Hybrid welding of additively manufactured and cast parts

M. Krochmal[1,a], A. Nammalvar Raja Rajan[2], G. Moeini[2], S. V. Sajadifar[1], T. Wegener[1], T. Niendorf[1]

[1] Institute of Materials Engineering – Metallic Materials, University of Kassel, Mönchebergstraße 3, 34125 Kassel, Germany
[2] Institute of Mechanical Engineering, Westphalian University of Applied Sciences, Neidenburger Straße 43, 45897 Gelsenkirchen, Germany
[a] Address all correspondence to this author. e-mail: krochmal@uni-kassel.de

Received: 28 July 2022; accepted: 14 November 2022; published online: 7 December 2022

Welding and joining of hybrid components consisting of additively manufactured (AM) parts and conventionally processed parts offer new opportunities in structural design. In the present study, AlSi10Mg specimens were fabricated using two different manufacturing processes, i.e., laser-based powder-bed fusion of metals (PBF-LB/M) and casting, and welded by means of friction stir welding (FSW). Material strength of dissimilar welded joints was found to be governed by the as-cast material, which is characterized by a very coarse microstructure resulting in inferior hardness and tensile properties. During fatigue testing, cast-cast specimens performed slightly better than their hybrid AM-cast counterparts with respect to lifetime, being rationalized by most pronounced strain inhomogeneities in the AM-cast specimens. With the aim of cost reduction, FSW can be employed to fabricate graded large parts as long as the AM as-built material is placed in the region demanding superior cyclic load-bearing capacity.

Introduction

Additive manufacturing (AM) is developing steadily in the last years as it allows to overcome challenges related to conventional manufacturing processes based on a tool free near-net shape production of components directly from three-dimensional (3D) model data [1]. This new kind of processing has provided unprecedented possibilities for industries to produce components with complex freeform geometries, where such geometries are not achievable using conventional manufacturing techniques [2, 3]. Among various types of AM processes, powder-bed based AM technologies represent the most promising candidates for producing complex components with good geometrical accuracy. However, the main challenge of these processes is the limited size of the build chamber, and therefore, the limitation in terms of dimensions of produced components. Thus, the part size limitation of AM components using powder-bed techniques leads to the necessity to employ welded component design, i.e., parts consisting of the combination of an AM component and a conventionally manufactured part (i.e., cast, milled), the latter being manufactured in large volume at much lower cost. In this regard, there is still a considerable lack of data (from modeling and experiments) related to investigations on the weldability and joinability of AM components as well as the structural integrity and reliability of their welded joints, especially hybrid joints consisting of AM parts and conventionally processed parts. This conclusion holds true for all metallic alloys considered in AM so far.

Considering lightweight structures, aluminum (Al) alloys have gained most attention as materials for fabrication of complex structures processed by laser-based powder-bed fusion of metals (PBF-LB/M). The inherited complex thermal history consisting of repeated melting, rapid solidification, and multiple reheating cycles accruing during the PBF-LB/M process, leads to grain refinement and formation of unique silicon (Si) networks resulting in superior mechanical behavior as compared to as-cast alloys [1]. The precipitation-hardenable AlSi10Mg alloy represents one of the commonly used Al alloys with respect to PBF-LB/M AM techniques [4–6]. It is well known that the mechanical properties of AlSi10Mg alloy are highly dependent

on the morphology and size of Si precipitates [7]. Rapid solidification can significantly influence the distribution of eutectic Si and, thus, affect the mechanical performance of AlSi10Mg alloys. In contrast, traditional casting processes are known to be characterized by low cooling rates, therefore, resulting in acicular or spherically shaped Si as a consequence [7]. Considerable differences in the microstructure of AM AlSi10Mg as compared to conventional as-cast material were already reported numerously, e.g., in [7]. Due to the different rates of solidification and cooling as well as the intrinsic heat treatment, an ultrafine supersaturated Si network forms during AM processing. Such cell-like structures so far were only found in AlSi10Mg specimens fabricated via PBF-LB/M, whereas distribution of brittle lamellar β-Al5FeSi was highlighted in as-cast specimens instead. As a result of the unique cellular structure of Si in AM Al-Si alloys, the toughness can be enhanced simultaneously [8].

The weldability of AM components is one of the main issues for industrial application to fabricate hybrid structures with unlimited sizes and also complex geometries in an economical way. Previous studies show the feasibility of fusion-welding processes, like laser welding [9] and electron beam welding [10] to join PBF-LB/M Al components. Microstructural results revealed a high percentage of porosity in the weld zone. However, the use of optimal welding parameters, such as a lower welding speed, can result in a larger weld pool and a lower cooling rate leading to degassing of the melt and, thus, minimal porosity [9]. To prevent detrimental aspects such as deterioration of material properties and porosity in the weld area, pressure welding provides for the possibility of achieving a sound welded joint. Among the solid-state joining processes, friction stir welding (FSW) was reported to be a promising joining technique for the welding of AM components [4, 11–14]. Accordingly, El Hassanin et al. [15] successfully applied FSW process for joining Ti6Al4V and AlSi10Mg specimens produced via PBF-LB/M. The achieved welded joints were free from macroscopic defects and revealed a significant decrease in porosity in both weld and heat-affected zone (HAZ) compared to the base material. Prashanth et al. [16] applied friction welding for joining of Al-12Si components produced by PBF-LB/M. Their investigation showed hardness degradation in the weld zone compared to the base material caused by the transformation of the cellular Si network into Si particles. Another investigation by Zhao et al. [17] confirmed this finding and introduced the effect of severe plastic deformation (SPD) during friction stir processing (FSP) on the spheroidization of the fine cellular networks of Si precipitates leading to significantly reduced tensile strengths in the processed area. In recent studies published by some of the present authors [4, 11, 18], the microstructure-property–performance relationships of friction stir-welded/processed Al components produced by PBF-LB/M were studied. The results showed that FSW/FSP can significantly affect the microstructure, namely grain size as well as precipitation morphology and distribution in the welded zone resulting in remarkable changes in mechanical behavior and integrity of welded joints. Considering the findings presented in the different studies [4, 9–11, 15–20], there is still a considerable lack of information on the microstructural evolution and its direct effect on the mechanical behavior of hybrid-welded joints. This especially holds true in case of FSW of AM AlSi10Mg components with as-cast counterparts. Thus, it is necessary to conduct comprehensive research on this topic in order to allow for production of cost-efficient, geometrically complex and tailored hybrid components being characterized by a safe and reliable response under complex loads. Completely different microstructural features in the as-cast and the AM components result in various mechanical performances and, hence, FSW can be exploited to tailor microstructure and mechanical properties of Al alloys by fabricating graded parts following a cost-efficient approach.

Results and discussion

Microstructural evolution

Figure 1 shows representative optical microscopy (OM) micrographs captured in the cross sections of similar and dissimilar FSW joints. In general, the images show clean welds without any signs of hot cracks or porosities. For the welds displayed in (a) and (c), a wave-like structure on the advancing side (AS) can be seen, which is in line with literature reporting on similar weld zones in [4] and [21]. It is well documented that SPD in FSW leads to the transportation of matter, leaving these wavy features in both the thermo-mechanically affected zone (TMAZ) and the stir zone (SZ) [21, 22]. Here, by direct comparison of the similar and dissimilar joints in (a) and (c), the differing initial material conditions become visible. The retreating side (RS), which is subjected to a material condition change, is characterized by an entirely different appearance. In (b), the cast-cast specimen does not show any wave-like structures on the AS and, moreover, generally features a rather consistent SZ. It is also worth noting that scan tracks are evident in the microstructure of the AM parts, while FSW caused dissolution of such tracks. This can be also linked to the SPD and the concomitant increase of temperature during FSW [4].

Electron backscatter diffraction (EBSD) inverse pole figure maps (IPF) of a hybrid-welded specimen are displayed in Fig. 2. In the AM part [(a)], the typical microstructure known from literature [4, 23], being characterized by clearly recognizable melt pools and no overall preferred orientation, is formed. The microstructure of the AM specimen consists of coarse columnar grains and some equiaxed grains with average grain sizes of approximately 14 and 11 µm, respectively. Coarse grains are formed in the center of melt pools, while

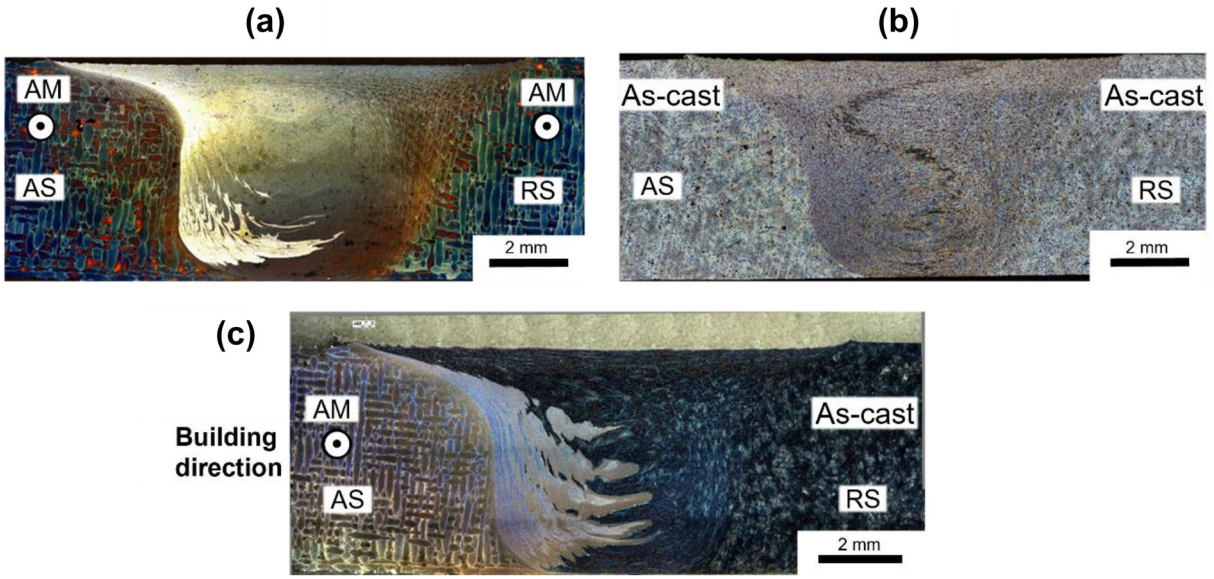

Figure 1: (a) Cross section of FSW AM specimens [4]; (b) cross section of FSW as-cast specimens; (c) FSW cross section of AM and as-cast specimens' hybrid joint.

equiaxed grains are introduced in the melt pool boundaries revealing changes in thermal gradient [24]. The growth direction of columnar grains is parallel to the building direction, pinpointing the strong impact of heat flow and thermal gradient in the final microstructure of this alloy processed via PBF-LB/M. Similar to the findings of Moeini et al. [4], the weld zone in (c) features a severely deformed microstructure being characterized by major grain refinement and random grain orientations. The grains in the stir zone are in a size range of approximately 1 to 3 µm and show slight elongation towards the top right corner. Similar to [4], formation of grain clusters with similar orientations can be seen and rationalized by the plastic flow and heat input of the weld process [25]. In contrast, the IPF map of the as-cast part in (b) shows coarse grains with diameters of more than 1 mm. The material features large second-phase particles that are similar in size to some of the largest grains found in the as-built part, highlighting the disparity between the two welding partners. Figure 3 highlights the composition of these precipitates in the as-cast condition and the FSW zone. After casting (a), both Si-rich, identifiable by their black color in the secondary electron (SE) image, and Mn-Fe-rich particles (white) form irregular patterns. Si particles appear in elongated needle-like shapes with lengths of up to 200 µm, indicating insufficient eutectic modification [26] as a result of low cooling rates, whereas the Mn-Fe particle formation does not seem to follow a general pattern. According to Seifeddine et al. [27], investigating differently cast AlSi10Mg, both a fine microstructure as well as small and favorably distributed iron-bearing phases and Si particles govern the strength and ductility of cast Al-Si-Mn alloys. Compared to the very fine Si networks present in AM-fabricated AlSi10Mg [23], the particles seen in Fig. 3(a) are rather coarse and arranged randomly. Thus, along with the significantly larger grain size, an overall weaker material response of the as-cast part has to be expected.

After welding and the associated SPD, the precipitations in (b) are broken into significantly smaller parts, ranging in size from approximately 1 to 20 µm. In addition, as a consequence of SPD, their shapes and proportions are changed due to partial dissolution, resulting in equiaxed appearances and reduced sizes for both the Si and Mn-Fe particles. Changes in the AM condition are in line with previous findings by Moeini et al. [4], reporting on dissolution and transformation of the eutectic Si networks initially present in AM AlSi10Mg when subjected to FSW. It is thought that in the stir zone, particles from the AM as well as from the as-cast side are shuffled and rearranged forming patterns as seen in Fig. 3(b).

Mechanical properties

Micro-hardness

Figure 4 displays micro-hardness mappings across both a hybrid AM-cast and a cast-cast specimen. The left AM part in (a) is characterized by an almost homogeneous hardness of 120 HV0.1, while the as-cast part on the right side, except occasional hotspots presumably due to the coarse Si-rich particles, exhibits hardness values in the range of 50 to 85 HV0.1. The weld zone shows an

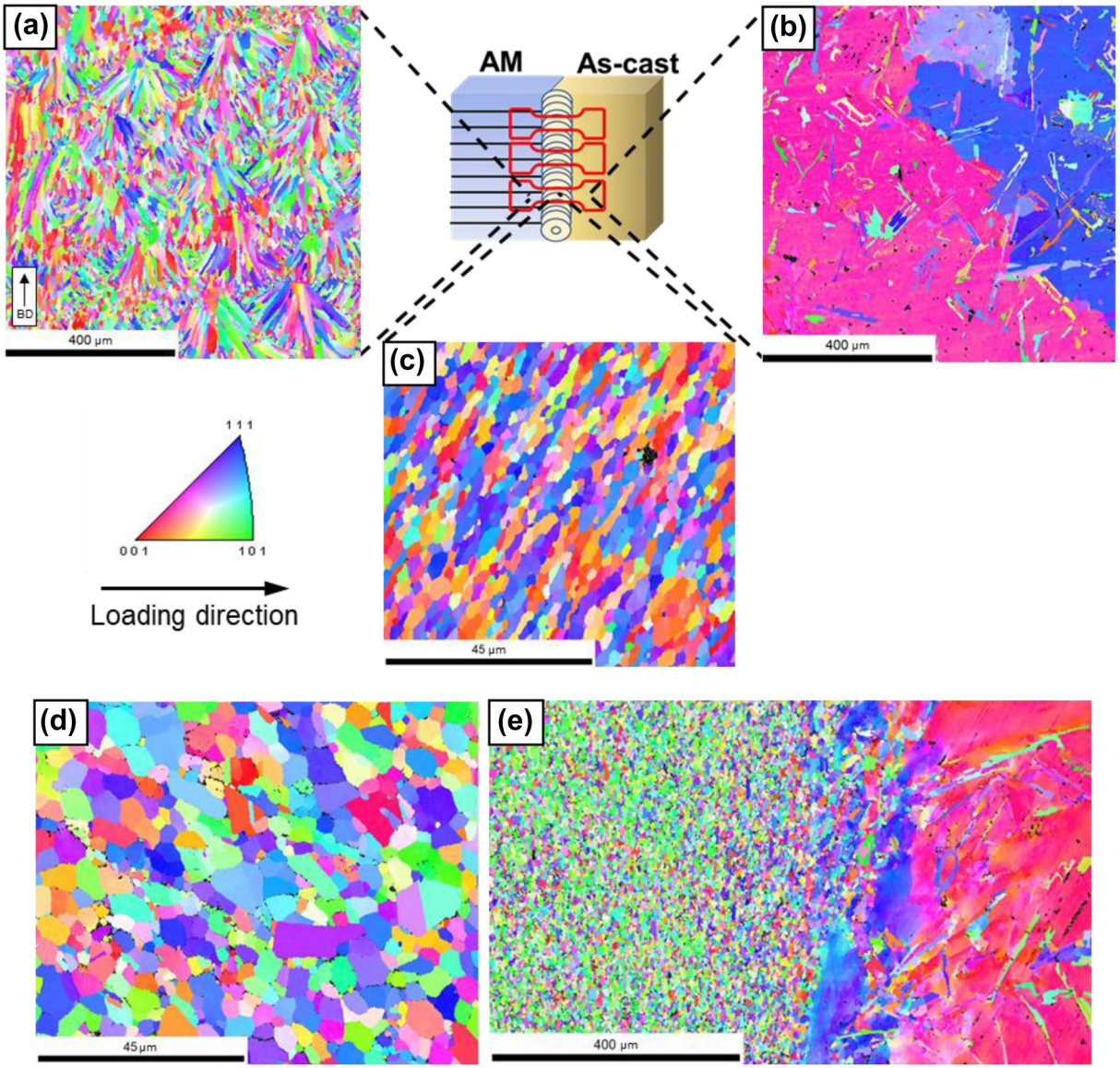

Figure 2: EBSD IPF maps depicting the different material states discussed in this work: (a) AM part (building direction (BD) is marked), (b) as-cast part, (c) magnified AM-cast weld zone, (d) magnified cast-cast weld zone, (e) transition from cast part to weld zone. Grain orientations are plotted with respect to the loading direction (being horizontal as indicated in the schematic).

intermediate hardness for the wave-like structures discussed above, while hardness in the remaining welded zone was found to be similar to the as-cast material. For the cast-cast specimen in (b), the weld zone features similar base hardness values in direct comparison to both of the as-cast specimens, however, also a notable absence of hotspots. A decrease in SZ hardness to about 80 HV0.1 was also observed by Moeini et al. [4] for hybrid AM-AM specimens. Surprising softening of the SZ, despite the grain refinement, was attributed to the dissolution, agglomeration, and subsequent rearrangement of the Si-rich networks [11] being initially present in AM AlSi10Mg and responsible for the high hardness and strength of the as-built condition.

Comparing the two weld zones, the cast-cast specimen exhibits lower hardness values (i.e., 50 HV0.1) compared to that of the AM-cast joint. To explain this phenomenon, further investigations considering the weld zone microstructure have been conducted by means of EBSD as displayed in Fig. 2(d) and (e). The left map in (d) shows random texture as a result of SPD, including fragmentation and recrystallization of the initial microstructure as has been discussed earlier [cf. Fig. 2(c)]. By comparing the IPF maps in (c) and (d), it can be deduced that the equiaxed and recrystallized grains introduced in the SZ of the AM-cast joint appear to be much finer compared to the cast-cast specimen. Compared to casting, the significantly

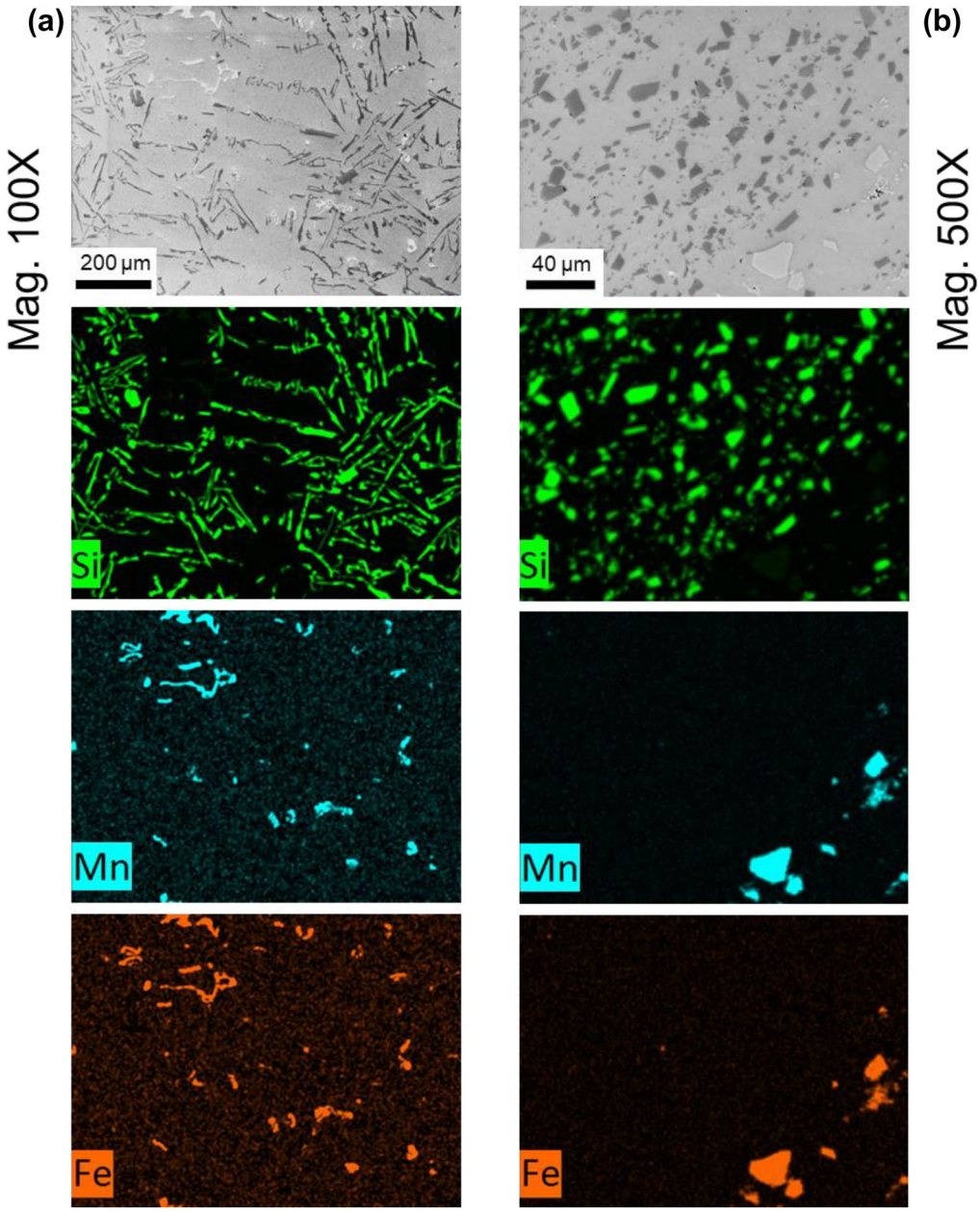

Figure 3: SE micrographs and corresponding energy-dispersive X-ray spectroscopy (EDS) elemental maps depicting (a) the structure of as-cast precipitates and (b) partly dissolved and rearranged precipitates in the FSW zone as a result of SPD.

finer AM microstructure seems to promote the formation of smaller grains inside the SZ when compared to cast-cast weld zones. This, in turn, explains the higher SZ hardness within the wave-like structures being present in the AM-cast specimen due to more efficient grain boundary strengthening. Furthermore, the inclusion of finely distributed Si particles stemming from the well-known PBF-LB/M Si networks seems to contribute. The cast-cast TMAZ in Fig. 2(e) is characterized by a distinct borderline towards the as-cast material on the right. Here, a single about 200 µm wide, differently oriented grain separating the material condition zones is seen. As this area features a rather soft orientation shift towards the base material, a second grain originating from the source material can be ruled out as origin and it has to be assumed that this buffer zone forms during the welding procedure as a result of plastic material flow at the SZ border. Further investigations into the mechanisms at play when welding the mentioned material combinations are still required, as assessment of the influence of individual process variables, e.g., welding temperature, is beyond the scope of present work.

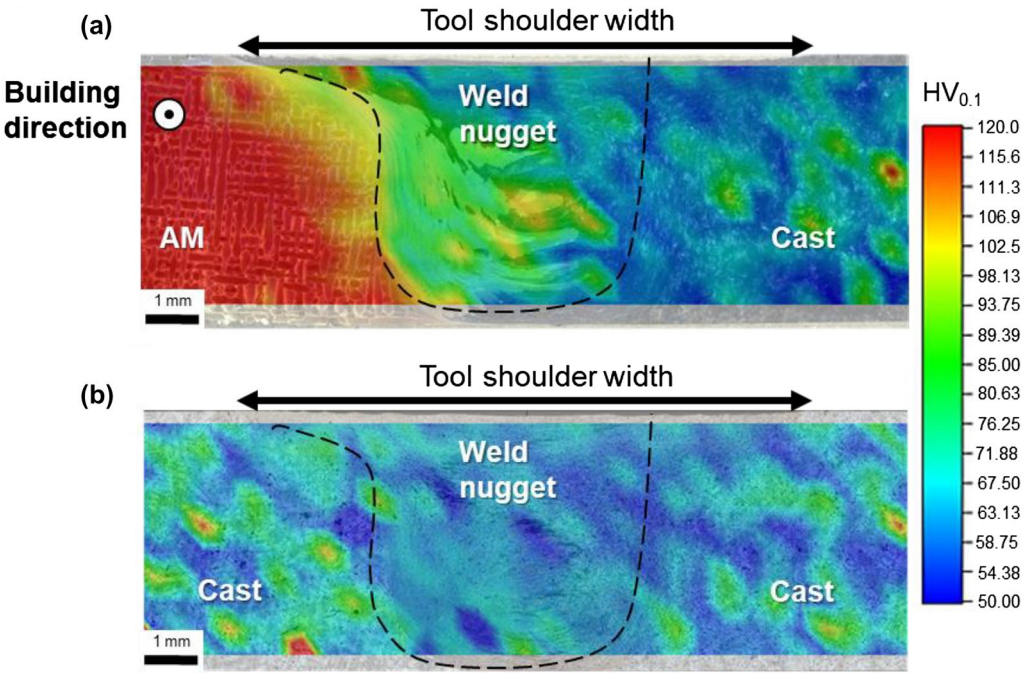

Figure 4: Micro-hardness mapping of the weld cross section of (a) FSW AM-cast and (b) FSW cast-cast.

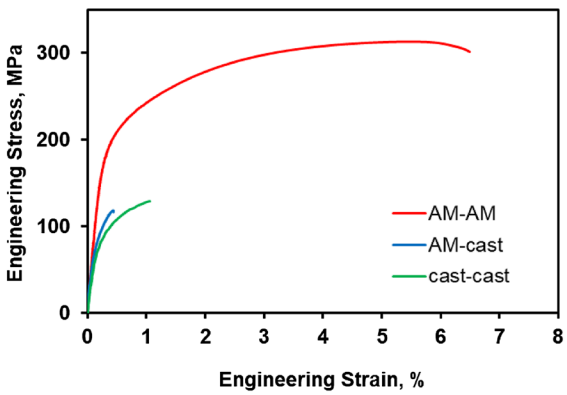

	AM-AM	AM-cast	cast-cast
UTS, MPa	285 287 313 310	84 118 54 61	129 130 128 127
EF, %	2.3 2.34 6.49 5.57	0.22 0.44 0.19 0.13	1.06 0.99 0.88 0.9

Figure 5: Tensile properties (UTS and EF) of the three hybrid FSW combinations across AM and cast specimens. AM-AM data were recompiled from [4].

Quasi-static behavior

The behavior under monotonic tensile loading is shown in Fig. 5. Representative stress-strain curves are displayed for the conditions considered, i.e., AM-AM, cast-cast, as well as AM-cast. Data for the AM-AM condition were recompiled from [4], with respect to the building direction used in this study. For the sake of brevity, only one of the tensile tests is plotted for each condition. Both ultimate tensile strength (UTS) and elongation to failure (EF) can be deduced from the results shown. As testing showed scatter for some of the conditions, a table containing all acquired results is attached to the diagram. By comparing tensile properties of different conditions, the AM-AM specimen displays the best results by a large margin, featuring a UTS of over 300 MPa and EF of more than 6%. The specimens involving as-cast parts exhibited adverse tensile properties, i.e., very low UTS values (less than 130 MPa) with EF values lower than 2%. EF was measured to be around 1% for the cast-cast joint and 0.5% for the AM-cast specimen. These results appear similar to the findings of Seifeddine et al. [27] for AlSi10Mg processed by sand casting. Inhomogeneous microstructure of cast components was reported to be the main reason for the inferior mechanical properties [27]. The formation of brittle and coarse intermetallic phases, e.g., β-phase needles during casting, led to the inhomogeneous microstructure. These coarse intermetallic phases deteriorate the mechanical properties of the alloy as they are sites prone to stress concentration and crack initiation. Very recently, Neuser et al. [28] also concluded that the solidification rate has a large impact on the mechanical properties of cast AlSi10Mg. Therefore, the relatively low UTS and EF values obtained in the present work can be attributed to the formation

of coarse and brittle secondary phases during the slow solidification process, caused by the large mold used in this study.

It was already shown by Moeini et al. [4] that friction stir-welded AM-AM specimens with similar building direction are characterized by inferior tensile and fatigue performances compared to their as-built counterparts. This was attributed to the coarsening and agglomeration of the fine Si networks in the SZ acting as the crack initiation point. Additionally, dissolution of the continuous Si network degraded the mechanical performance inside the significantly deformed weld zone, leading to localized material softening. Analogously, the present study also features inhomogeneous specimens; however, this time the as-cast base material acts as a weak point, always being the failure-initiating zone. Here, it is expected that the SZ with ultrafine microstructure possesses superior tensile properties compared to the coarse as-cast material. In order to validate these expectations, additional tensile tests have been conducted and monitored using digital image correlation (DIC). Figure 6(a) depicts the results obtained for a hybrid AM-cast specimen at a load level being close to failure. The color code represents the vertical strain on the visible specimen surface. Results clearly indicate a heterogeneous strain response. The upper and middle parts, representing the AM and weld zones, respectively, are characterized by up to 10 times lower strain values as compared to the as-cast part below. Particularly high strains can be seen in the middle of the as-cast material, already highlighting the final crack initiation zone. Specimen failure was observed as brittle, with no obvious necking around the fractured region. Fracture initiation during fatigue testing was found to exclusively occur in one of two distinct areas, i.e., close to the weld zone or at the radius below [cf. Fig. 6(b)]. Specimen geometries like the one used in present work are known to feature slightly varying stress levels across their gauge length as a result of notch effects [29]. Accordingly, crack initiation always occuring at the two distinct spots mentioned is likely to be a superimposed effect of microstructural inhomogeneities and geometrical notches. In case of the specimens studied here, such effects create unfavorable stress fields in the microstructurally weak as-cast region. For clarity, these considerations are schematically summarized in Fig. 6(b), also highlighting the observed crack initiation points with regard to the material combinations considered.

Low-cycle fatigue (LCF) behavior and fracture analysis

Cyclic deformation responses (CDRs) of both cast-cast as well as AM-cast specimens are shown in Fig. 7. In order to counteract effects stemming from material and strain heterogeneity as efficiently as possible, all tests were conducted using an extensometer with a gauge length of 10 mm, monitoring almost the entire specimen gauge volume. Three specimens have been fatigued for every condition and stress amplitude of which only one specimen is presented in the following for the sake of brevity. As no pronounced scatter was observed with respect to resulting stress amplitudes for a given strain amplitude, the CDRs presented can be seen as representative. For the strain amplitude of 0.2%, one CDR being representative for the AM-AM condition (with the building direction (0°-0°) as recompiled from [4]) is depicted, demonstrating the considerable difference in specimen lifetime. No further testing of AM-AM parts (i.e., for all loading amplitudes lower than 0.2%) was considered here as lifetimes would not be within the LCF regime. Furthermore, increasing stress amplitudes up to the fifth cycle, which can be deduced for all the specimens tested, do not represent material response but rather the control characteristic of the used testing machine as the load was increased stepwise during the first few cycles in order to avoid buckling of the miniature specimens. Generally, all CDRs of specimens containing as-cast material are almost equal, irrespective of the conditions and strain amplitudes considered (slight cyclic hardening in all cases).

It is expected that such cyclic hardening can be traced back to an increase in dislocation density due to the local plastic deformation as has been reported for LCF testing of different alloys by Niendorf et al. [30] and Zhang et al. [31]. However, experimental proof is currently missing and will be subject of future work. Figure 8(d) and (e) shows the evolution of the plastic strain in dependence of the number of cycles. Results shown indicate more intense plastic deformation and cyclic hardening for the cast-cast specimens compared to the AM-cast joint. Cyclic plastic strain amplitudes of the cast-cast joint are about 50% higher than those of the AM-cast counterpart (e.g., when comparing the initial values for 0.15%) owing to the different material combinations being present inside the volume probed by the extensometer [cf. schematic depicted in Fig. 6 (b)]. The effect of various conditions on fatigue life will be detailed and discussed in the following paragraph. The aforementioned cyclic specimen behavior can be rationalized by the results obtained by tensile testing. As is shown in Fig. 5, data revealed significantly lower yield stresses for the welded specimens containing as-cast base material. For the AM-cast specimens, most of the plastic strain likely is present in the as-cast region with the AM base material featuring predominantly elastic deformation. Consequently, the AM part, experiencing primarily elastic strain at these loads, detrimentally affects the cyclic response as it contributes less to total strain as compared to the as-cast material at a given load. This, in turn, results in increased stress amplitudes as the as-cast part has to contribute proportionally larger amounts of strain in case of the hybrid specimens. The higher plastic strain being seen in case of the cast-cast specimens results from the larger as-cast material volumes contributing to the overall plastic strain amplitude at a given stress. Half-life hysteresis loops of the specimens shown in Fig. 8 as well reveal that cyclic plasticity is slightly different in cast-cast and AM-cast

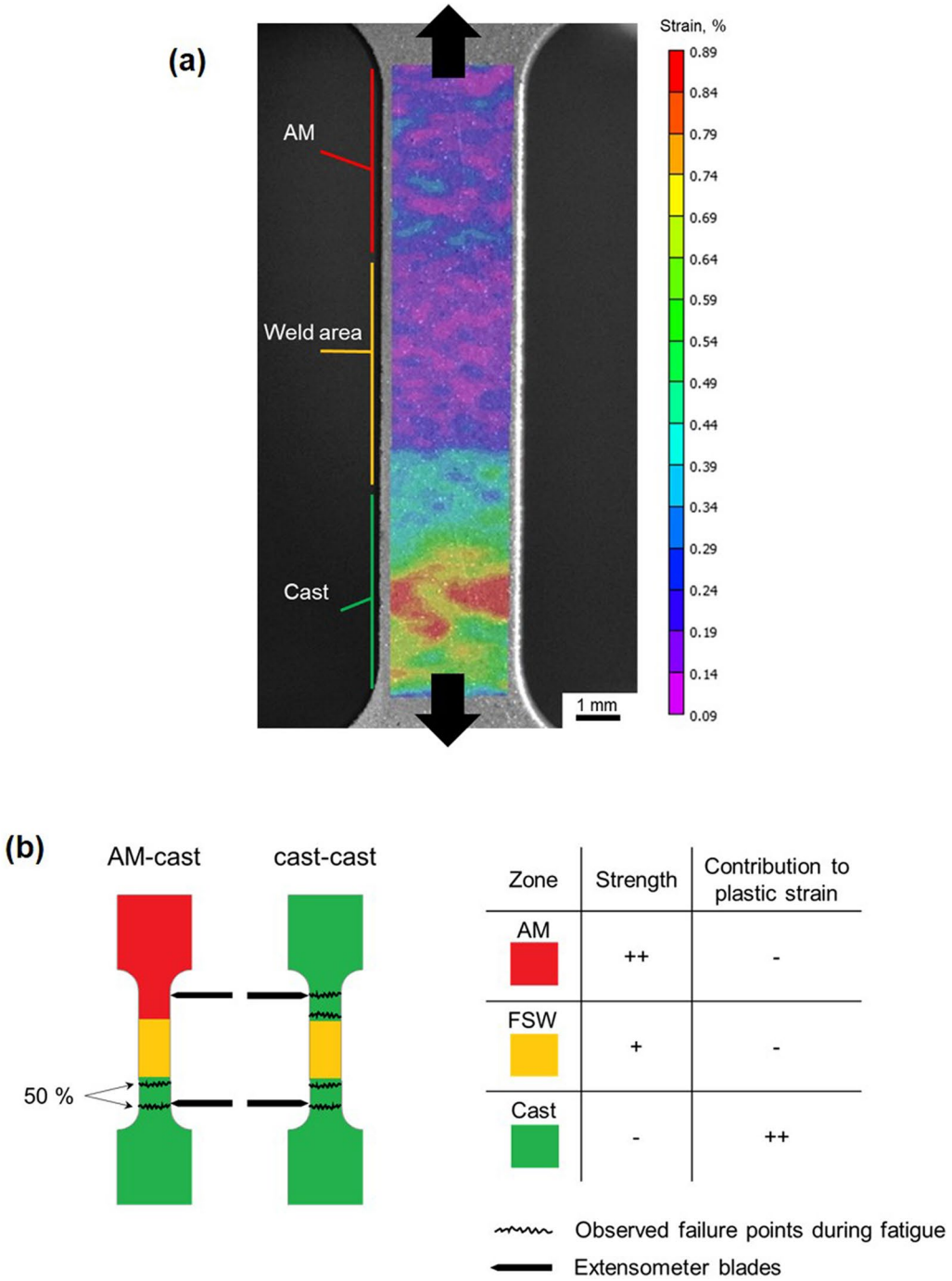

Figure 6: (a) Strain calculations (vertical direction) for an AM-cast specimen during tensile testing and (b) a schematic overview summarizing the different material zones, properties, and failure initiation points as well as positioning of the extensometer blades.

specimens, with higher values seen in the cast-cast condition. The area of a hysteresis loop is an indicator for the energy dissipation per cycle. Thus, this characteristic can be linked to the dislocation activity and cyclic plastic deformation [32, 33]. By comparing stress amplitudes of both conditions based on the half-life hysteresis loops, it can be deduced that the cast-cast joints generally experienced slightly lower stress amplitudes than AM-cast specimens, which again is an indication of lower deformation resistance being rationalized by the inferior base material strength.

An overview of all tested specimens and their respective number of cycles to failure is given in Fig. 7. Especially the

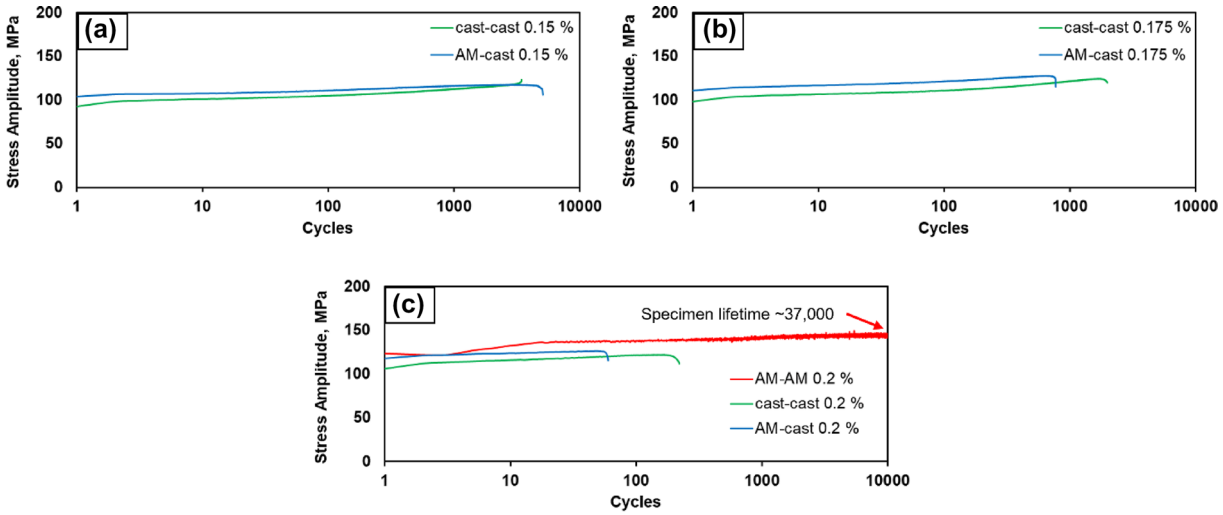

	0.15 %	0.175 %	0.2 %
AM-cast	805 5 136 14 084	414 773 1 447	33 60 202
cast-cast	2 794 3 463 4 830	1 980 2 059 4 281	54 221 325

Figure 7: Cyclic deformation responses of hybrid cast-cast and AM-cast specimens at constant total strain amplitudes of (a) 0.15%, (b) 0.175%, and (c) 0.2%. For comparison, a part of the CDR of an AM-AM specimen, recompiled from [4], is also shown in (c). Total specimen lifetime (cycles to failure) for all fatigue tests conducted is shown in the attached table.

AM-cast condition suffers from exceptional lifetime scatter (805 to 14.084 cycles for a total strain amplitude of 0.15%), which complicates LCF data interpretation. Generally, the cast-cast condition demonstrates better fatigue performance with lower overall scatter; however, the difference is not significant enough (e.g., lifetimes for 0.15%) to be considered indisputable. The results obtained in the present study have to be compared with data available in the literature. Basically, hybrid joints containing as-cast material experience drastically reduced LCF lifetimes compared to the as-built specimens [34, 35] or AM-AM joints [4]. As has been discussed earlier, the as-cast region acts as the weakest link and is, therefore, responsible for the early fatigue failures in large parts. It is widely known that during cyclic deformation of cast Al alloys, defects such as porosities, oxides, intermetallic phases, inclusions, and second-phase particles being present in the microstructure influence the fatigue response [36–42]. Consequently, the large second-phase particles seen in the present study as well as oxide films developing during casting facilitate crack initiation and growth by creating local stress fields around themselves, eventually leading to rapid failure. This effect becomes most obvious at high total strain amplitudes and high plastic strain amplitudes, respectively, and eventually reduces fatigue lifetime to less than 100 cycles. Here, the pronounced lifetime scatter for AM-cast specimens can be rationalized through the smaller absolute volume fraction of the as-cast material [contributing to the entire specimen gauge volume, cf. Fig. 6 (b)] compared to the cast-cast condition. Eventually, the former specimen locally experiences proportionally higher plastic strains in the weak material than the individual as-cast zones in the cast-cast specimen do. Accordingly, failure mechanisms are affected by the random distribution of second phases in the relatively small as-cast region, finally promoting more pronounced lifetime scatter. Consequently, the cast-cast condition exhibits slightly better fatigue performance due to less localized plastic strain in the as-cast parts. As a result, the beneficial contribution of a more stable AM microstructure seems to be offset by the higher stress amplitudes as a direct result of strain-controlled testing. Consequently, more plastic deformation in the weak as-cast region of the hybrid parts results in the relatively poor fatigue performance highlighted. Microstructural observations and the assessment of mechanical behavior in present work show that, despite lower overall strength, hybrid joints can still be employed to manufacture larger components with graded mechanical properties with high cost efficiency. However, special attention has to be paid to heterogeneity of the parts realized to ensure structural stability. It can be deduced from

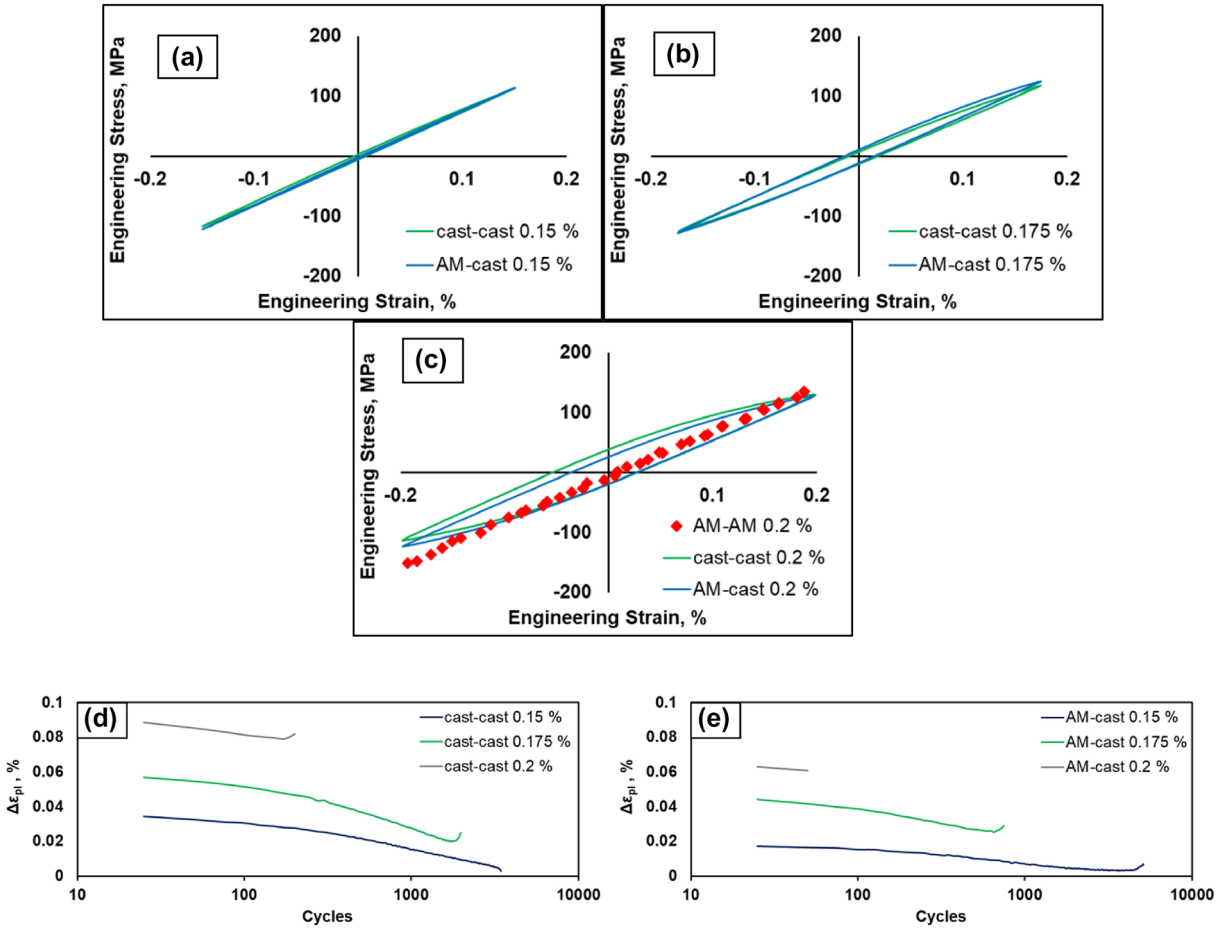

Figure 8: Half-life hysteresis loops of hybrid cast-cast and AM-cast specimens at constant strain amplitudes of (a) 0.15%, (b) 0.175%, and (c) 0.2%. For comparison, an AM-AM hysteresis loop, recompiled from [4], is also shown in (c). (d) and (e) display the cyclic plastic strain response of the three cast-cast specimens and AM-cast specimens, respectively. Data were collected every 25 cycles.

data shown that the AM material can be used for the side of the component where superior mechanical properties, i.e., high strength and good ductility, are required. Such aspects have to be adapted in the design of hybrid components. Additionally, optimizations of the microstructure, e.g., through heat treatment, have to be explored in future work in order to adjust the weak as-cast material, however, without detrimentally affecting the properties of the AM part.

Representative fracture surfaces of fatigued specimens are shown in Fig. 9. For the sake of brevity, only AM-cast specimens are illustrated, as cast-cast specimens are characterized by identical fracture behavior and surfaces. As has been discussed before, failure of all specimens was observed in the as-cast base material, being characterized by rapid and brittle crack growth crossing the few grains being present in the specimen cross section. The fracture surfaces themselves are characterized by a rather smooth appearance indicating transcrystalline crack growth. Well-known features of fatigued specimens, i.e., areas being related to fatigue crack initiation and propagation characterized by sub-micron fatigue striations as well as an final overload fracture area, cannot be derived. Especially for the specimens being fatigued at total strain amplitudes of 0.15 and 0.175%, elongated notch-type defects can be seen throughout the fracture surface, supporting the theory of crack initiation at elongated second-phase precipitations. This is in line with data available in literature. Fan et al. [43] used a computational finite element-based approach, and concluded that large particles led to concentrations of plastic strain. This resulted in a more pronounced microstructural sensitivity towards the high-cycle fatigue regime. The involvement of coarse eutectic Si plates and needles (as a result of insufficient eutectic modification) in cracking is also documented in [44]. Chan et al. [45] demonstrated the microstructural dependence of cast B319 Al and found that fatigue crack growth occurred starting from multiple crack initiation sites. Influencing factors on crack initiation were pores, particle fracture, and rapid crack growth along interdendritic cell boundaries. As no signs of crack propagation in certain directions could be found in the present study, it is

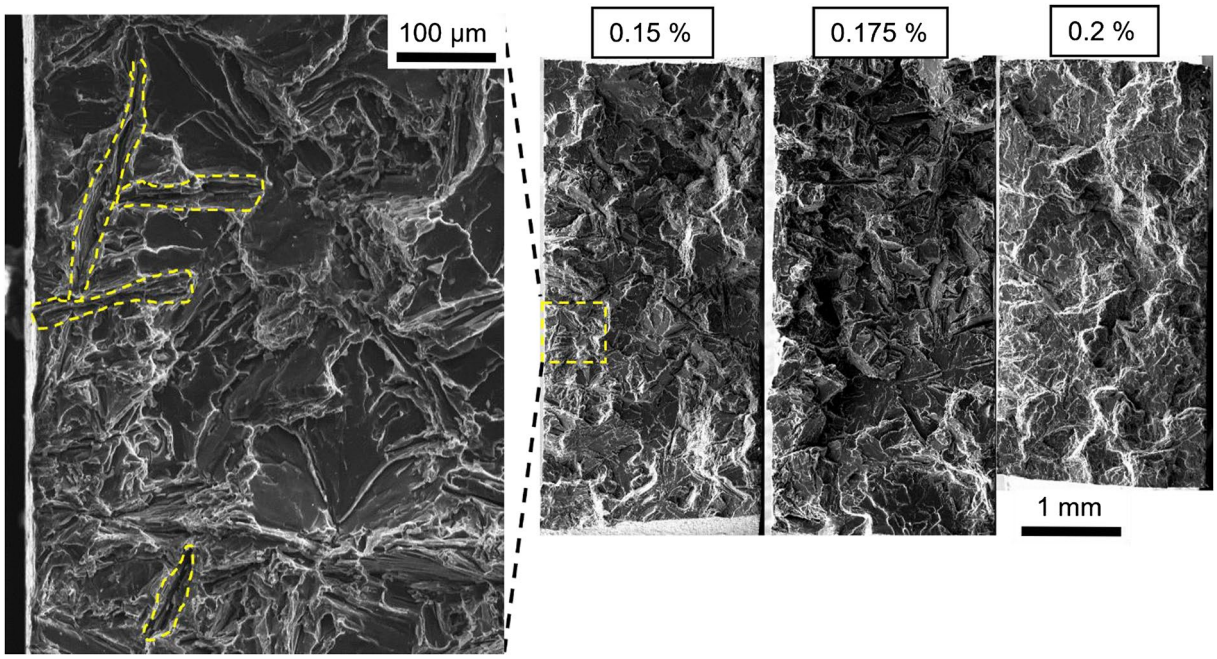

Figure 9: Representative fracture surfaces after LCF testing at varying total strain amplitudes collected from three hybrid AM-cast specimens using scanning electron microscopy (SEM). Strain amplitudes are noted in the individual overview pictures.

assumed that multiple crack initiation processes occurred in parallel and once a critical load had been reached, the remaining material failed rapidly, eventually creating fracture surfaces almost resembling those from tensile testing. The influence of aforementioned precipitations seems to decrease with increasing stress amplitudes as the specimen tested at 0.2% only depicts a few elongated notches, indicating a shift in failure mechanisms towards the ultra-low-cycle fatigue regime.

Summary and conclusions

Two different manufacturing processes have been employed to create AlSi10Mg specimens, i.e., laser-based powder-bed fusion of metals and conventional casting. Using friction stir welding, the two material conditions were joined, eventually representing a hybrid joint. In order to analyze the microstructure, scanning electron microscopy as well as optical microscopy were used. Mechanical properties were characterized by means of microhardness testing, tensile experiments, and strain-controlled low-cycle fatigue tests. The key findings can be summarized as follows:

1. The as-cast material is characterized by inferior hardness and a very coarse microstructure compared to its AM counterpart. Depending on the welding partners (i.e., cast-cast or AM-cast), hardness values, grain size, and the overall appearance of the weld zone changed. Tensile testing and digital image correlation measurements revealed that deformation is localized in the as-cast region of the AM-cast specimens. When directly comparing the different specimens, the cast-cast condition shows slightly better tensile properties.
2. During fatigue tests, the as-cast region governs the strength and lifetime of the hybrid specimens. As a result, both specimen conditions are characterized by a rather similar cyclic deformation response. The cast-cast specimen showed slightly better total fatigue lifetimes. This is attributed to most pronounced deformation inhomogeneities, being extremely detrimental in terms of strain and damage localization, in the hybrid AM-cast specimen.
3. Fracture surface analysis reveals rapid, brittle crack growth, resulting in rather smooth surfaces featuring elongated notches. It is deduced that crack initiation is promoted by large second-phase particles throughout the specimen cross section. Thus, adapted post-process heat treatments will allow for optimization of properties. Such treatments have to strengthen the cast part without detrimentally affecting the additively manufactured part.
4. Results obtained clearly reveal that friction stir welding can be employed for the fabrication of large, defect-free graded components at high cost-efficiency. However, damage localization in the relatively weak as-cast part has to be avoided. In order to strengthen the hybrid joint, not only post-welding heat treatments will be an option. Due to the high load-bearing capacity of the as-built condi-

tion, AM specimens can be used in the region of the final component, where higher cyclic loading is applied. Thus, advanced design of hybrid components represents another potential option.

Experimental procedure

Components of AlSi10Mg alloy were manufactured using different processes, namely AM and gravity die casting. The AM specimens were produced using a commercially available SLM system SLM 280^{HL} (SLM Solutions, Lübeck, Germany). The machine is equipped with two lasers, one of them being the 400 W Yb:YAG fiber laser employed in the present work. Commercially available powder material AlSi10Mg (wt%) was used to manufacture the AM specimens under inert conditions, i.e., in argon environment. The parameters used for manufacturing the specimen volume were: scanning speed of 1170 mm/s, power of 400 W, layer thickness of 60 µm, and hatch spacing of 0.2 mm. The AM specimens with a size of 150 mm × 40 mm × 5 mm were manufactured according to the schematic displayed in Fig. 10(a). As-cast specimens were manufactured using material with a similar nominal chemical composition (AlSi10MnMg (wt%)) in gravity die casting. In this alloy, Mn serves to improve the castability [46]. The material was first cast into a mold featuring a base area of 700 × 200 mm^2, an area of 710 × 210 mm^2 at the top and a height of 100 mm. Afterwards, the casting was milled to sheets with a size of 150 mm × 40 mm × 5 mm, equal to the AM specimens. Similar (cast-cast) and dissimilar (AM-cast) material combinations were welded in a butt-joint configuration [cf. Fig. 10(b)] using FSW with a rotational speed of 800 rotations/min and a travel speed of 400 mm/min. In order to avoid material pre-shifting, the angle between pin and specimen surface was set to 2°, which is frequently applied for welding of Al alloys. For the hybrid welds, an offset of 1 mm towards the as-cast material was applied. This was done to promote a high density in the welded area, while the AM part of the joint still was plasticized 1.5 mm into the nugget area. The stir tool was made from hot work steel X40CrMoV5-1 and featured a shoulder diameter of 12 mm and a pin with a metric M5 thread. The welding trials were carried out using appropriate clamping and fixing devices, respectively. All specimens were tested in the condition directly stemming from the process considered, i.e., no post-process heat treatments were considered. This procedure was chosen to investigate a worst-case scenario as material inhomogeneities were expected to be most detrimental in this as-welded state. Considerations of post-welding heat treatments were out of scope of the present study and will be subject of future work.

For microstructural characterization of the weld cross section, OM and SEM were used. SEM investigations were conducted on a Zeiss ULTRA GEMINI high-resolution microscope being equipped with an EDS detector and an EBSD unit. This SEM was also used for the analysis of the fracture surfaces. The specimens were prepared by mechanical grinding and polishing according to standard procedures. Keller's

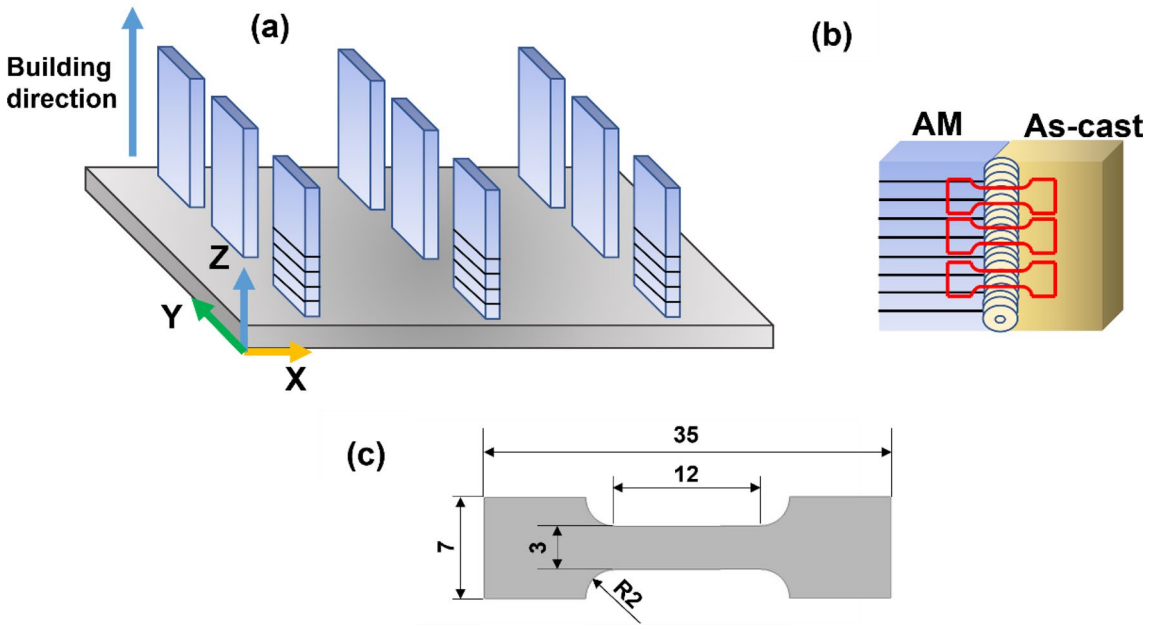

Figure 10: (a) Schematic illustration of the AM specimens processed by PBF-LB/M and (b) exemplary specimens joint by FSW. The orientation of AM specimens relative to the welding direction is shown by the black lines. The superimposed schematic highlights the position of the specimens used for characterization. (c) Dimensions of tensile and fatigue specimens having a thickness of 2.0 and 1.5 mm, respectively. See text for details.

reagent was used to etch the specimens for OM analysis. Vickers micro-hardness mapping was performed using a KB 30 S hardness tester. A force of 1 N (HV 0.1) was applied for 10 s for each single indent on the cross-sectional surface of the welded specimen according to the standard ASTM: E384-11e1. The center-to-center distance between the indents was 0.2 mm in the x-direction and 0.3 mm in the y-direction.

For mechanical characterization, specimens were cut using electro discharge machining with their long axis oriented perpendicular to welding direction. Afterwards, specimens were mechanically ground down to a grit size of 15 µm for tensile and fatigue tests, in order to remove any surface residue. Tensile tests were conducted using flat dog-bone-shaped specimens with gauge section dimensions of 12 mm × 3 mm × 2 mm as displayed in Fig. 10(c). The tensile tests were carried out at room temperature (RT) using an MTS793 test rig in displacement control under a crosshead speed of 2 mm/min corresponding to a nominal strain rate of 0.004 1/s (calculated on basis of the specimen gauge length). Four specimens were tested per condition.

The LCF experiments were carried out utilizing a digitally controlled servo-hydraulic test rig (MTS Bionix) with a maximum force capacity of 25 kN under fully reversed push-pull loading ($R_\varepsilon = -1$) at a constant strain rate of 0.006 s^{-1} and at constant total strain amplitudes of 0.15, 0.175, and 0.2%. A MTS extensometer with a gauge length of 10 mm was used to measure and control strain. Three LCF tests per condition were performed on flat dog-bone shaped specimens being characterized by gauge section dimensions of 12 mm × 3 mm × 1.5 mm at RT. The specimen geometry employed was numerously used in literature (e.g., [33, 47–49]) but, however, has not been captured by an official standard. In order to further assess the material behavior, additional tensile tests have been conducted and analyzed using DIC. These tests were carried out with a constant crosshead speed of 0.25 mm/min and interruptions every 0.005 mm in order to take images of the specimen surface for subsequent strain calculation using VIC-2D (Correlated Solutions) with a subset size of 111 px and a step size of 5 px. Pictures were recorded using a digital reflex camera (Nikon D3200) equipped with a macro lens (AF-S Nikkor 105 mm/2.8G IF-ED) being capable of taking photos with a resolution of 24.1 Megapixels. Speckle patterns were applied using a paintbrush (after the specimen had been ground down to a grit size of 5 µm and subsequently polished manually). Sufficient illumination during testing was ensured using common halogen spotlights.

Acknowledgments

Authors would like to thank the German Research Foundation (DFG) for financial support within the Project No. 450156756. Furthermore, Ms. Julia Richter is thanked for preparation of the AM specimens.

Funding

Open Access funding enabled and organized by Projekt DEAL.

Data availability

The dataset generated during the presented study is available upon request from the corresponding author.

Declarations

Conflict of interest The authors declare that they have no known competing financial or personal interests that could have influenced the work reported in this document.

Open Access

References

1. B. Chen, S.K. Moon, X. Yao, G. Bi, J. Shen, J. Umeda, K. Kondoh, Scr. Mater. **141**, 45 (2017). https://doi.org/10.1016/J.SCRIPTAMAT.2017.07.025
2. C.Y. Yap, C.K. Chua, Z.L. Dong, Z.H. Liu, D.Q. Zhang, L.E. Loh, S.L. Sing, Appl. Phys. Rev. **2**, 41101 (2015). https://doi.org/10.1063/1.4935926
3. J. Zhang, B. Song, Q. Wei, D. Bourell, Y. Shi, J. Mater. Sci. Technol. **35**, 270 (2019). https://doi.org/10.1016/j.jmst.2018.09.004
4. G. Moeini, S.V. Sajadifar, T. Wegener, C. Rössler, A. Gerber, S. Böhm, T. Niendorf, J. Mater. Res. Technol. **12**, 1446 (2021). https://doi.org/10.1016/j.jmrt.2021.03.101
5. A. Mertens, J. Delahaye, O. Dedry, B. Vertruyen, J.T. Tchuindjang, A.M. Habraken, Procedia Manuf. **47**, 1089 (2020). https://doi.org/10.1016/j.promfg.2020.04.121
6. F. Trevisan, F. Calignano, M. Lorusso, J. Pakkanen, A. Aversa, E.P. Ambrosio, M. Lombardi, P. Fino, D. Manfredi, Materials (2017). https://doi.org/10.3390/ma10010076
7. Q. Yan, B. Song, Y. Shi, J. Mater. Sci. Technol. **41**, 199 (2020). https://doi.org/10.1016/j.jmst.2019.08.049

8. J. Suryawanshi, K.G. Prashanth, S. Scudino, J. Eckert, O. Prakash, U. Ramamurty, Acta Mater. **115**, 285 (2016). https://doi.org/10.1016/j.actamat.2016.06.009
9. C. Emmelmann, P. Sander, J. Kranz, E. Wycisk, Phys. Procedia **12**, 364 (2011). https://doi.org/10.1016/j.phpro.2011.03.046
10. M. Nahmany, I. Rosenthal, I. Benishti, N. Frage, A. Stern, Addit. Manuf. **8**, 63 (2015). https://doi.org/10.1016/j.addma.2015.08.002
11. G. Moeini, S.V. Sajadifar, T. Wegener, F. Brenne, T. Niendorf, S. Böhm, Mater. Sci. Eng. A **764**, 138189 (2019). https://doi.org/10.1016/j.msea.2019.138189
12. Z. Du, M.J. Tan, H. Chen, G. Bi, C.K. Chua, Weld World **62**, 675 (2018). https://doi.org/10.1007/s40194-018-0585-7
13. F. Scherillo, A. Astarita, U. Prisco, V. Contaldi, P. Di Petta, A. Langella, A. Squillace, Metallogr. Microstruct. Anal. **7**, 457 (2018). https://doi.org/10.1007/s13632-018-0465-y
14. Z. Du, H.-C. Chen, M.J. Tan, G. Bi, C.K. Chua, J. Manuf. Process. **36**, 33 (2018). https://doi.org/10.1016/j.jmapro.2018.09.024
15. A.E. Hassanin, C. Velotti, F. Scherillo, A. Astarita, A. Squillace, L. Carrino, in *2017 IEEE 3rd International Forum on Research and Technologies for Society and Industry* (*RTSI*), IEEE (2017), p. 1
16. K.G. Prashanth, R. Damodaram, S. Scudino, Z. Wang, K. Prasadao, J. Eckert, Mater. Des. **57**, 632 (2014). https://doi.org/10.1016/j.matdes.2014.01.026
17. L. Zhao, J.G. Santos Macías, L. Ding, H. Idrissi, A. Simar, Mater. Sci. Eng. A **764**, 138210 (2019). https://doi.org/10.1016/j.msea.2019.138210
18. G. Moeini, S.V. Sajadifar, T. Engler, B. Heider, T. Niendorf, M. Oechsner, S. Böhm, Metals **10**, 85 (2020). https://doi.org/10.3390/met10010085
19. W.W. Wits, J.J. Becker, Procedia CIRP **28**, 70 (2015). https://doi.org/10.1016/j.procir.2015.04.013
20. A. Ascari, A. Fortunato, E. Liverani, A. Gamberoni, L. Tomesani, Phys. Procedia **83**, 839 (2016). https://doi.org/10.1016/j.phpro.2016.08.087
21. M. Besel, Y. Besel, U. Alfaro Mercado, T. Kakiuchi, Y. Uematsu, Int. J. Fatigue **77**, 1 (2015). https://doi.org/10.1016/j.ijfatigue.2015.02.013
22. M. Cabibbo, A. Forcellese, E. Santecchia, C. Paoletti, S. Spigarelli, M. Simoncini, Metals **10**, 233 (2020). https://doi.org/10.3390/met10020233
23. L. Thijs, K. Kempen, J.-P. Kruth, J. van Humbeeck, Acta Mater. **61**, 1809 (2013). https://doi.org/10.1016/j.actamat.2012.11.052
24. J. Richter, S.V. Sajadifar, T. Niendorf, Addit. Manuf. **47**, 102346 (2021). https://doi.org/10.1016/j.addma.2021.102346
25. R.L. Xin, B. Li, Q. Liu, MSF **654–656**, 1195 (2010). https://doi.org/10.4028/www.scientific.net/MSF.654-656.1195
26. O. Gursoy, G. Timelli, J. Mater. Res. Technol. **9**, 8652 (2020). https://doi.org/10.1016/j.jmrt.2020.05.105
27. S. Seifeddine, T. Sjgren, I.L. Svensson, Metall. Sci. Technol. *25* (2007)
28. M. Neuser, O. Grydin, Y. Frolov, M. Schaper, Prod. Eng. Res. Dev. (2022). https://doi.org/10.1007/s11740-022-01106-1
29. T. Niendorf, Diss., Ermüdungseigenschaften ultrafeinkörniger kubisch raumzentrierter Werkstoffe: Einfluss der Mikrostruktur (2010)
30. T. Niendorf, C. Lotze, D. Canadinc, A. Frehn, H.J. Maier, Mater. Sci. Eng. A **499**, 518 (2009). https://doi.org/10.1016/j.msea.2008.09.033
31. Z. Zhang, Z. Hu, S. Schmauder, M. Mlikota, K. Fan, J. Mater. Eng. Perform. **25**, 1650 (2016). https://doi.org/10.1007/s11665-016-1977-8
32. S.V. Sajadifar, G.G. Yapici, E. Demler, P. Krooß, T. Wegener, H.J. Maier, T. Niendorf, Int. J. Fatigue **122**, 228 (2019). https://doi.org/10.1016/j.ijfatigue.2019.01.021
33. S. Picak, T. Wegener, S.V. Sajadifar, C. Sobrero, J. Richter, H. Kim, T. Niendorf, I. Karaman, Acta Mater. **205**, 116540 (2021). https://doi.org/10.1016/j.actamat.2020.116540
34. S. Romano, L. Patriarca, S. Foletti, S. Beretta, Int. J. Fatigue **117**, 47 (2018). https://doi.org/10.1016/j.ijfatigue.2018.07.030
35. C. Fischer, C. Schweizer, MATEC Web Conf. **326**, 7003 (2020). https://doi.org/10.1051/matecconf/202032607003
36. D. Ovono Ovono, I. Guillot, D. Massinon, J. Alloys Compd. **452**, 425 (2008). https://doi.org/10.1016/j.jallcom.2006.11.052
37. M. Tiryakioğlu, On fatigue life variability in cast Al–10%Si–Mg alloys. Mater. Sci. Eng. **527**, 1560 (2010)
38. Q.G. Wang, P.N. Crepeau, C.J. Davidson, J.R. Griffiths, Metall. Mater. Trans. B **37**, 887 (2006). https://doi.org/10.1007/BF02735010
39. G. Sigworth, Int. J. Metalcast. **5**, 7 (2011). https://doi.org/10.1007/BF03355504
40. Q. Wang, D. Apelian, D. Lados, J. Light Met. **1**, 85 (2001). https://doi.org/10.1016/S1471-5317(00)00009-2
41. Q. Wang, D. Apelian, D. Lados, J. Light Met. **1**, 73 (2001). https://doi.org/10.1016/S1471-5317(00)00008-0
42. M. Tang, P.C. Pistorius, Int. J. Fatigue **94**, 192 (2017). https://doi.org/10.1016/j.ijfatigue.2016.06.002
43. J. Fan, D.L. McDowell, M.F. Horstemeyer, K. Gall, Eng. Fract. Mech. **70**, 1281 (2003). https://doi.org/10.1016/S0013-7944(02)00097-8
44. Y. Birol, A.A. Ebrinc, Int. J. Cast Met. Res. **21**, 408 (2008). https://doi.org/10.1179/136404608X370747
45. K.S. Chan, P. Jones, Q. Wang, Mater. Sci. Eng. A **341**, 18 (2003). https://doi.org/10.1016/S0921-5093(02)00196-X
46. Rheinfelden AllOYS, Primary Aluminium Alloys for Pressure die Casting, https://rheinfelden-alloys.eu/wp-content/uploads/2016/01/05-HB-DG_Ci_Sf_Cm_Td_Ma_RHEINFELDEN-ALLOYS_2015_EN.pdf. Accessed 12 Oct 2022
47. T. Wegener, J. Koopmann, J. Richter, P. Krooß, T. Niendorf, Fatigue Fract. Eng. Mater. Struct. **44**, 2570 (2021). https://doi.org/10.1111/ffe.13527

48. T. Wegener, F. Brenne, A. Fischer, T. Möller, C. Hauck, S. Auernhammer, T. Niendorf, Addit. Manuf. **37**, 101603 (2021). https://doi.org/10.1016/j.addma.2020.101603
49. T. Wegener, J. Günther, F. Brenne, T. Niendorf, in *Structural Integrity of Additive Manufactured Parts*, ed. by N. Shamsaei, S. Daniewicz, N. Hrabe, S. Beretta, J. Waller, M. Seifi (ASTM International, West Conshohocken, 2020), p. 465. https://doi.org/10.1520/STP162020180108